ADVANCED FUNCTIONAL MATERIALS
www.afm-journal.de

Hierarchical Pore Structure Composite Electrode by Electrospinning for Dendrite-free Zinc-Based Flow Battery

*Pengfei Wang, Tao Peng, Yuhang Ban, and Menglian Zheng**

In the pursuit of sustainable energy solutions, zinc-based flow batteries stand out for their potential in large-scale energy storage, offering a blend of cost efficiency and safety. Although the porous electrode provides an increased specific surface area for reaction, the non-uniform deposition of zinc, attributed to uneven concentration distribution within the porous electrode, has been a pivotal issue in accelerating the formation of zinc dendrites, which hinders the enhancement of energy density. A composite electrode with a strategic hierarchical pore structure has been developed with aligned nitrogen-doped carbon fibers and traditional carbon felt. This structure takes advantage of the large pores of the carbon felt for efficient through-flow paths, ensuring higher flow rates, while the dual-scale pores within the electrospun film enhance mass transfer and increase the specific surface area. At 320 mA cm^{-2}, it achieved an ≈11.4% improvement in the battery's energy efficiency. Moreover, the nitrogen doping and the optimized reaction uniformity within the composite electrode have been instrumental in reducing the generation of zinc dendrites. The battery, integrated with the innovative composite electrode, maintained an energy efficiency of 59.2% at 320 mA cm^{-2} after 300 cycles, which is a substantial improvement in operational longevity.

1. Introduction

The quest for sustainable and efficient energy storage solutions has led to an increased focus on flow batteries, which offer distinct advantages over conventional battery technologies.[1] Notably, flow batteries are scalable, have a long cycle life, and can manage the storage of energy generated from intermittent renewable sources, such as solar and wind power, making them a compelling choice for grid energy storage applications.[2,3] Among the various chemistries being explored, zinc-based flow batteries stand out for their potential to provide a safe, cost-effective, and environmentally benign energy storage option.[4,5] Despite these benefits, the widespread adoption of zinc-based flow batteries is hindered by several technical challenges. One of the primary issues is the non-ideal behavior of the zinc electrode during charge–discharge cycles, which refers to the formation of zinc dendrites.[6] These phenomena can cause internal short circuits, rapid capacity fade, and, in the worst-case scenario, safety hazards, thereby limiting the battery's lifespan and reliability.[7]

Essentially, the increasing demand for increments in applied current density per active area of electrodes for decreasing the battery stack's cost per power capacity makes the use of porous electrodes an inevitable solution.[8] In zinc-based flow batteries, carbon-based porous electrodes, such as carbon cloth and carbon felt, are commonly utilized as the skeleton for zinc deposition.[9] Some other carbon electrodes will also be treated as electrode materials for zinc-based flow batteries.[10] These materials not only provide a larger specific surface area,[11] but also take advantage of their porous structure to provide ample space for zinc growth, particularly under high areal capacity conditions.[12] Plenty of previous studies have focused on the control interface characteristic of carbon materials, which typically involves a higher propensity for uneven nucleation and the growth of zinc dendrites.[13] An effective approach is the surface modification of the electrode or the fabrication of an artificial interface layer to induce uniform deposition of zinc.[14–16] Common types of interface layers include metallic materials,[17] polymeric materials,[18] carbon-based materials,[19] and so on.[20–23] Xie et al. used a network interface layer of copper-zinc alloy to stabilize the zinc anode interface and accelerate the reaction kinetics.[24] Wang et al. designed a reduced graphene interface layer based on Ag nanoparticle modification to achieve uniform and controlled zinc deposition.[25] Cui et al. used an artificial solid electrolyte interface phase composed of interconnected ZnO nanoparticles to achieve the function of zinc ion desolvation and limit two-dimensional diffusion.[26] Sui et al. formed a passivation layer on the surface of the zinc anode by passivation solution, inhibited the side reaction process, and

P. Wang, M. Zheng
State Key Laboratory of Clean Energy Utilization
Zhejiang University
Hangzhou 310027, China
E-mail: menglian_zheng@zju.edu.cn
P. Wang, T. Peng, Y. Ban, M. Zheng
Institute of Thermal Science and Power Systems
College of Energy Engineering
Zhejiang University
Hangzhou 310027, China
P. Wang, M. Zheng
Institute of Wenzhou
Zhejiang University
Wenzhou 325036, China

The ORCID identification number(s) for the author(s) of this article can be found under https://doi.org/10.1002/adfm.202409036

[Correction added on September 2, 2024, after first online publication: Author affiliations have been updated in this version.]

DOI: 10.1002/adfm.202409036

improved the uniformity of zinc deposition.[27] Nevertheless, less effort has been placed on understanding how electrode morphology affects zinc deposition and how to suppress zinc dendrites through restructuring carbon fibers as porous electrodes.

The intricate structure of the porous carbon-based electrode also poses adverse effects on the zinc deposition process.[28] Specifically, the non-uniformity of fibers within porous electrodes can result in the significant uneven distribution of electrolyte concentration and local current density, leading to disparities in the rate of zinc transportation,[29,30] and sequentially localized zinc ion depletion in the high current density zone. The increased concentration gradient accelerates the formation of zinc dendrites, which in turn exacerbates the uneven distribution of zinc ions and thus creates a more pronounced gradient that drives the growth of dendrites.[31] Therefore, to suppress the growth of zinc dendrites, it is critical to adjust the uniformity of concentration distribution within the electrode and to regulate the rate of ion transport. Achieving a uniform deposition process necessitates the optimization of the electrode's morphology to facilitate even electrolyte flow and current distribution, thereby minimizing the concentration gradients that can lead to dendritic growth. Lin et al. woven zinc powder and polymer into fibers with a three-dimensional structure. The dendrite growth was inhibited, and the uniformity of zinc deposition was improved.[32] Sun et al. constructed a uniform opportunity channel for zinc by using Cu-Sn nanowires while using the three-dimensional spatial structure to provide a buffer for volume changes during zinc deposition.[33] Zhuang et al. used a 3D porous copper skeleton to achieve uniform deposition of zinc and significantly reduce polarization loss.[34] However, to the best of our knowledge, none of the conventional porous electrodes, such as carbon felt, carbon paper, and carbon cloth, can meet the abovementioned contradictory technical requirements for suppressing zinc dendrite formation in zinc-based flow batteries. This calls for a novel but practical porous electrode structure that simultaneously possesses large permeability spaces, short diffusion pathways, and uniform channels (**Figure 1**). This structure enhances not only the permeation of electrolytes but also the diffusion of ions for smoothing zinc deposition under high current densities. Inspiration can be found in non-sedimentary flow batteries. Especially in all-vanadium flow batteries, researchers have carried out some successful designs for electrode structure optimization.[35–37]

The present study builds upon the existing body of work by introducing a novel composite electrode design that leverages the synergistic effects of aligned nitrogen-doped electrospun carbon fibers (ANECF) with the established performance of carbon felt (CF). The fabrication of ANECF employed electrospinning technology, which not only offered the advantages of low raw material and production costs but also enabled the precise manipulation of fiber alignment and pore size distribution. The dual pore size in ANECF provided a high surface area and a directed and fast pathway for ion transport, while nitrogen doping can effectively enhance the binding energy between zinc and fibers. Simultaneously, the parallel distribution of fibers and flow channels in the ANECF can improve the uniformity of active material distribution. By combining these features with the mechanical integrity and large pore structure of CF, this hierarchical pore composite electrode provided superior of performance attributes for zinc-based flow batteries. Additionally, the performance of batteries

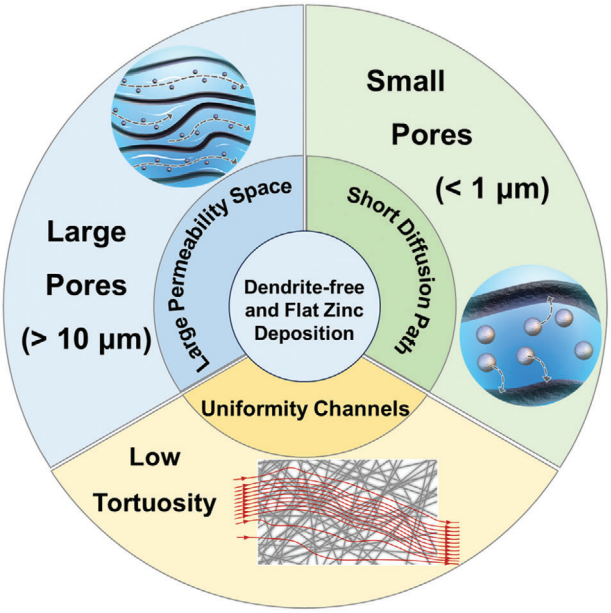

Figure 1. Pore structure required to achieve flat dendrite-free zinc deposition.

equipped with ANECF+CF was evaluated and demonstrated a notable improvement in terms of voltage efficiency, with an increase of 11.4% at a current density of 320 mA cm^{-2}. By suppressing the formation of zinc dendrites and side reactions, the lifespan of the battery was significantly extended. After 300 cycles, it still maintained an energy efficiency (EE) of 59.2%. These findings highlight the potential of ANECF+CF as a key material for advancing the efficiency and durability of zinc-based flow batteries, contributing to the development of sustainable energy storage technologies. The structural design approach presented was rather uncommon and innovative, addressing the issue of zinc deposition from a unique perspective. The main innovative aspects of this work are as follows:

i. Pore structure optimization for enhancing zinc deposition uniformity: Unlike previous studies that focused on protective layer materials, this work specifically addressed the influence of electrode's microstructure on the uniformity of zinc deposition at the anode of zinc-based flow batteries. Particularly at high current densities, this non-uniformity can lead to severe zinc dendrite formation and performance degradation. The experimental and simulation results confirmed the effectiveness and importance of optimizing the porous electrode's pore structure;
ii. One-step manufacturing method: This work employed a one-step manufacturing method that utilizes the self-adhesion phenomenon of fibers at a high viscosity and the directional distribution of fibers at high rotation speeds, achieving the fabrication of a dual-scale porous structure electrode at one single step. This method was simpler and more operable, avoiding the multi-step manufacturing processes or the use of various precursor solutions required for the fabrication of hierarchical porous structures in the past

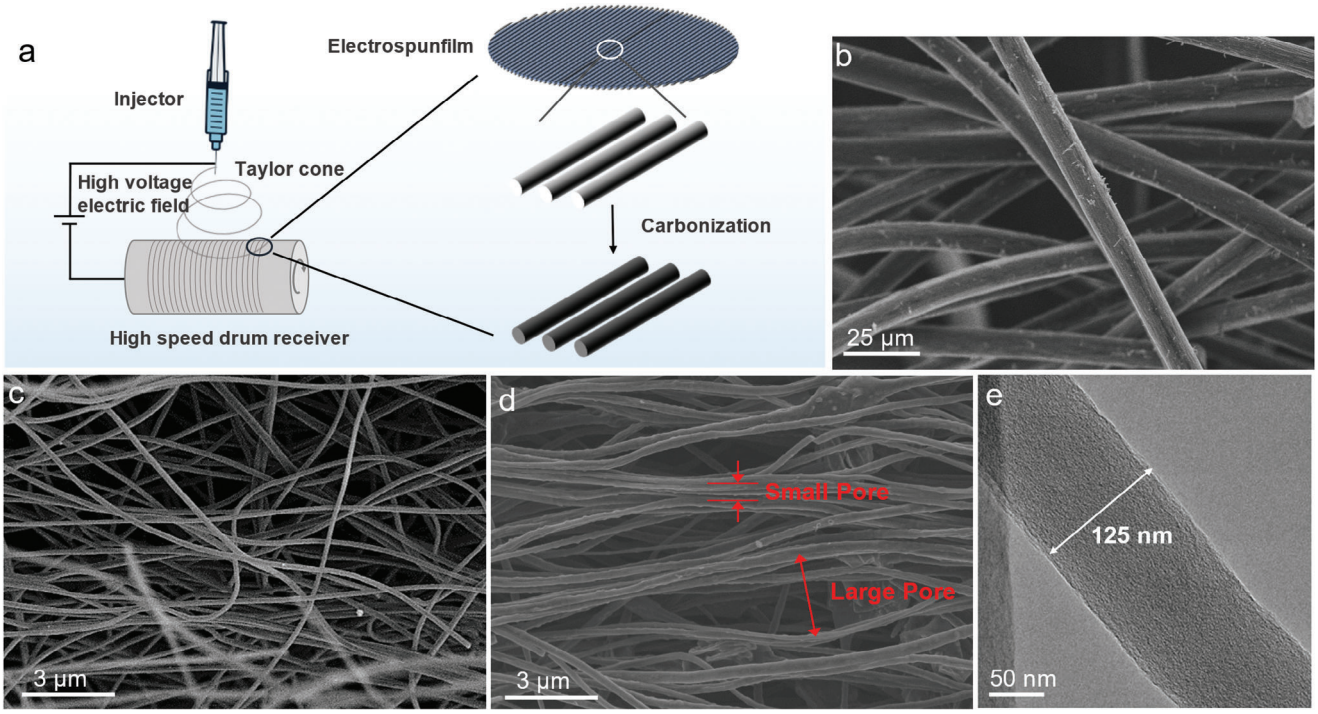

Figure 2. a) Schematic synthesis process of ANECF electrode. b) SEM image of CF. c) SEM image of ECF, d) SEM image of ANECF. e) TEM image of a single ANECF fiber.

iii. Uniqueness of pore structures in ANECF: The dual-scale pore structures within ANECF were positioned along the same flow path, with CF at the base providing a large permeation velocity, ensuring the full utilization of the pores at all levels. This addressed the issue of uneven pore structure and the lack of connectivity between pores of different sizes, which often resulted in the underutilization of the available pore structures.

2. Results and Discussion

In this work, the electrospinning technology was employed to fabricate ANECF in one step (**Figure 2a**). Polyacrylonitrile (PAN) formed a relatively orderly arranged fibrous film on the surface of a high-speed rotating drum. Upon carbonization, the fibers evolved into oriented carbon fibers. The fiber arrangement in electrospun carbon fiber (ECF) was similarly disordered to that of conventional CF, yet the diameter of the fibers and the size of the interstitial gaps differed. Compared to the traditional CF structure (as shown in Figure 2b), ANECF exhibited not only a more orderly arrangement but also a bimodal pore structure. In addition to the larger interstitial pores between the original fibers, aggregation of some fibers occurred, leading to the formation of smaller pores between them. This could be attributed to the presence of pyridinic nitrogen, which had an electron-withdrawing effect on the neighboring carbon atoms.[38] This one-step fabrication method was more convenient and easy to operate than the traditional multi-step fabrication method for a bimodal pore structure. Scanning electron microscopy (SEM) images revealed that many fibers aggregated significantly, creating fiber bundles reminiscent of carbon cloth (Figure 2c). The gaps within the fiber bundles were relatively small, while the spaces between the bundles were larger (Figure 2d). This morphological structure suggested the potential presence of pores across various scales within its interior. This characteristic was anticipated to exert an influence on its electrochemical performance. Furthermore, compared to CF, ANECF exhibited a smaller fiber diameter. Transmission electron microscopy (TEM) image indicated that the diameter of individual fibers in ANECF was ≈125 nm (Figure 2e). In contrast, the fiber diameter of traditional carbon felt could reach around 10 μm. This characteristic significantly increased the specific surface area of carbon fiber electrodes, which could enhance the electrochemical performance of the electrodes in energy storage applications.

Compared to ANECF, the arrangement of fibers in ECF more closely resembled that of conventional CF, with a relatively disordered distribution of fibers. However, the fiber diameter of ECF was similar to that of ANECF. X-ray diffraction (XRD) results indicated that both ECF and ANECF exhibited broader (002) peak widths, which may be attributed to the lower degree of graphitization due to limitations imposed by the low temperature in the tubular furnace under laboratory conditions (Figure S1, Supporting Information).

In addition to the differences in the microstructure, the elemental composition of ANECF and ECF also varied. The incorporation of melamine during the electrospinning process introduced nitrogen doping into the ANECF. X-ray photoelectron spectroscopy (XPS) results revealed a distinct nitrogen peak in the ANECF (**Figures 3a** and S3, Supporting Information). The XPS spectra of ECF showed almost no peak of N, indicating that it contains almost no nitrogen. This was consistent with the precursors used for ECF material, which only included

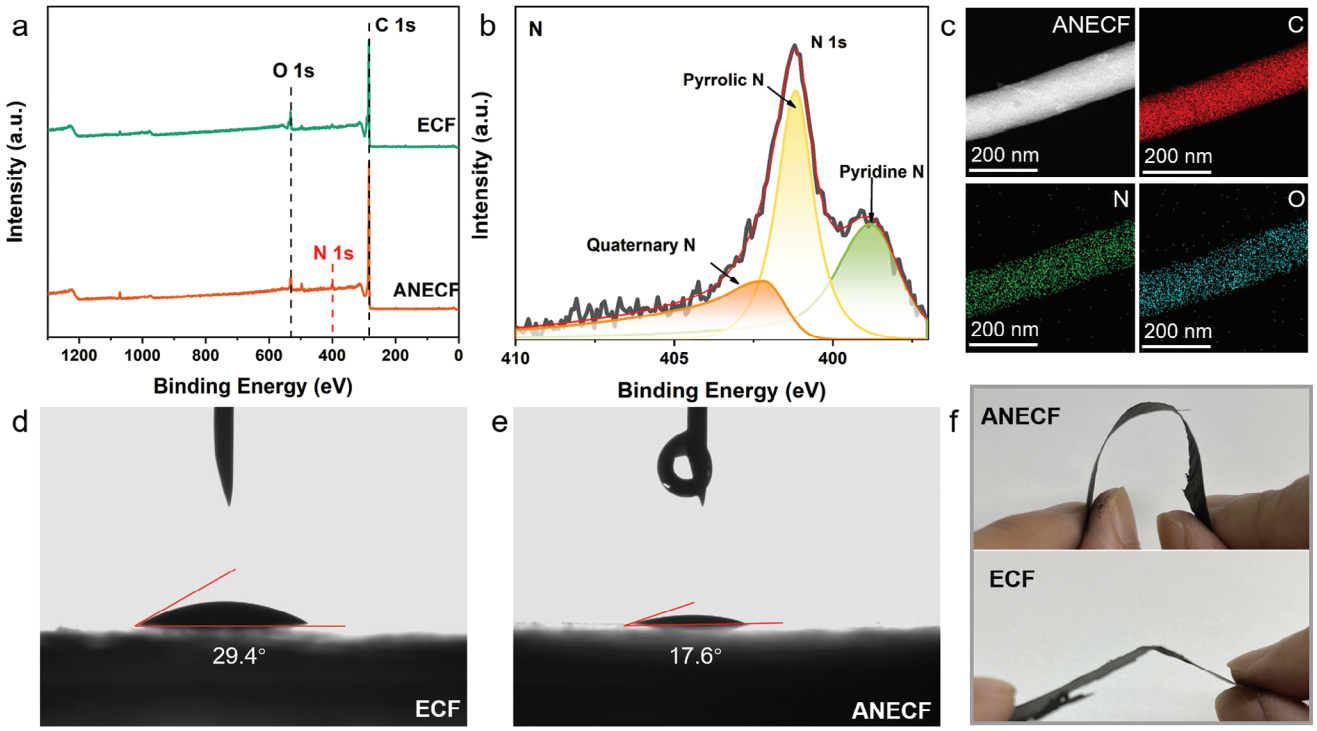

Figure 3. a) XPS of ECF and ANECF. b) N spectra of ANECF. c) EDS mapping of ANECF. Contact angle of d) ECF and e) ANECF. f) Photos after bending of ANECF and ECF.

N,N-dimethylformamide (DMF and PAN. The fitting results of the N 1s peak are depicted in Figure 3b. The fitting peaks at the binding energies of 398.83, 401.17, and 402.18 eV were attributed to pyridinic nitrogen, pyrrolic nitrogen, and quaternary nitrogen, respectively, with pyridinic and pyrrolic nitrogen being the predominant species. Currently, it is widely accepted among researchers that pyridinic and pyrrolic nitrogen exhibit stronger binding energy with zinc atoms.[39–41] Therefore, ANECF holds promise for regulating the zinc deposition process at the electrode interface and suppressing the formation of zinc dendrites. The successful incorporation of nitrogen was further confirmed by the energy dispersive spectrometer (EDS) mapping (Figure 3c), which showed that the nitrogen content in ANECF was ≈3% (Table S1, Supporting Information). The introduction of nitrogen to some extent improved the surface properties of the electrospun carbon fibers, as nitrogen-containing functional groups increased the surface polarity of the carbon fibers, enhancing their interaction with water molecules. Figure 3d,e demonstrated that ANECF exhibited a smaller contact angle, thereby proving the improvement in its hydrophilicity. Additionally, the incorporation of nitrogen enhanced the flexibility of the electrospun films. While ECF tended to fracture upon bending, ANECF could bend at larger angles or even twist without breaking (Figure 3f). To more precisely elucidate the variations in the mechanical properties of the material, tensile tests were conducted (Figure S4, Supporting Information). The findings indicated that ANECF (2858 MPa) exhibited superior mechanical performance, with Young's modulus that is twice that of ECF (1438 MPa). ANECF demonstrated an enhanced capacity to withstand greater deformations without undergoing fracture. This increased flexibility allowed it to maintain structural integrity when being compressed in flow batteries to the differences in microstructure, the pore structure of electrospun carbon fibers differed significantly from that of carbon felt. To further validate the pore structure captured through SEM, additional analyses and characterizations were conducted. Mercury intrusion porosimetry (MIP) was utilized to characterize the pore size distribution of the different materials. As shown in **Figure 4a**, traditional CF had a very large pore size of ≈120 µm, while the pore size of ECF was only 800 nm. Smaller pores are beneficial for reducing the diffusion distance of ions toward the electrode surface, thereby enhancing mass transfer effects. However, it can also lead to decreased permeability and uneven distribution of reactants, which may result in greater pump power consumption for flow batteries. In comparison to ECF, the pore size distribution curve of ANECF exhibited two distinct peaks, representing the presence of pores of two different sizes, 1 µm and 100 nm, within the material. This was attributed to the aggregation of some fibers within the electrode, where some inter-fiber spaces were closer together and others were more separated, transforming the original 800 nm pores into two-size pores. The pore size distribution curve confirmed the presence of two types of pores within the ANECF. This finding strongly supports the results observed in the SEM images. Compared to the ECF with a permeability of 985 mDarcy, the ANECF exhibited a significantly higher permeability of 14528 mDarcy when the porosity was basically unchanged. This enhanced permeability facilitated the infiltration of the electrolyte within the electrode matrix and expedited the transport of active ions to the reaction sites. The uneven distribution of reactants in electrospun fibers would also

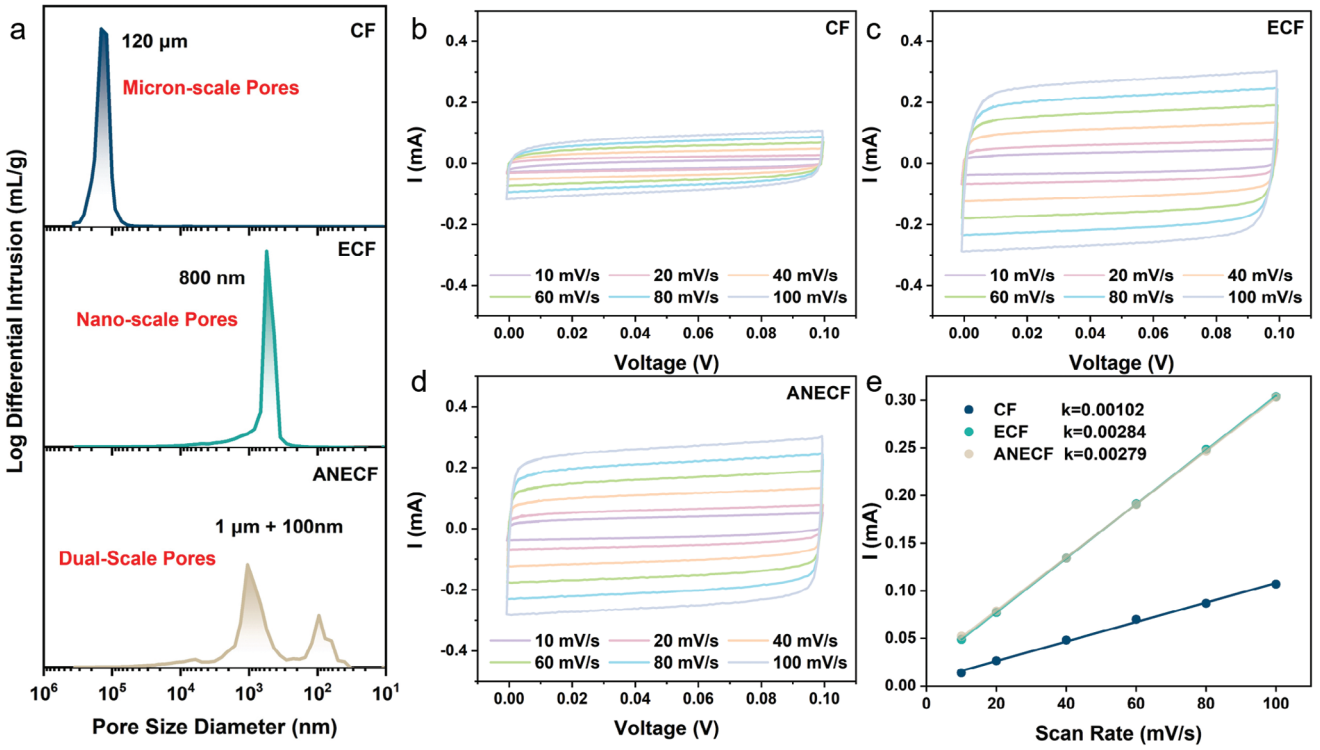

Figure 4. a) Pore size distribution measured by MIP of CF, ECF, and ANECF. CV curves at different scan rates of b) CF, c) ECF, and d) ANECF. e) Plot of current versus scan rate at 0.1 V.

be improved. The substantial increase in the permeability was primarily attributed to the altered arrangement of fibers. The more orderly fiber alignment resulted in a more streamlined and direct internal flow channel, with a reduction in tortuosity from 6.03 to 1.98 (Table S2, Supporting Information).

In addition to pore size, the specific surface area of the materials was also tested. Due to the fact that the electrochemical specific surface area (ECSA) more accurately reflected the kinetic performance of an electrode compared to the physical surface area measured by the BET method, the ECSA was measured as an alternative to the physical specific surface area obtained by using the BET method. Cyclic voltammetry (CV) curves of the three materials at different scan rates were measured (Figure 4b–d). By linearly fitting the current at 0.1 V and the scan rate (Figure 4e), the slope of the fitted line represented the double-layer capacitance of the material, i.e., the ECSA. The results indicated that the slopes of ECF and ANECF were essentially similar, and their specific surface areas were consistent, confirming that changes in the pore structure between fibers did not affect their specific surface area. ECSA measurements indicated that ECF and ANECF have comparable ECSAs, demonstrating that the secondary pores are not formed on the fiber surface but are created by the gaps between fibers. This also corroborates the porous structure proposed based on SEM observations. The ECSA of CF was only one-third that of ECF or ANECF. Considering that the samples had the same area (1 cm * 1 cm) and that electrospun carbon fibers were thinner and lighter in weight when normalized to the same weight, the ECSA of ECF and ANECF would be nearly 90 times higher than that of CF. The enhanced surface area provided more sites for ion transfer and reaction, thereby facilitating a more uniform distribution of current and minimizing the concentration gradients that could lead to non-uniform zinc plating and dendritic growth.

Pores as small as 100 nm were instrumental in facilitating the rapid mass transfer of zinc ions on the fiber surface. To substantiate this conclusion, electrochemical impedance spectroscopy (EIS) tests were conducted to measure the impedance of different electrode materials. The EIS plot was composed of two distinct parts: the semicircle in the high-frequency region represents the charge transfer impedance of the battery, with a smaller diameter indicating a lower charge transfer impedance. The straight line in the low-frequency region denotes the ion diffusion impedance at the electrode–electrolyte interface, where a steeper slope signifies a lower ion diffusion impedance. EIS results indicated that the Nyquist plots of both ANECF and ECF exhibited a higher slope in the low-frequency region compared to CF, signifying a lower diffusion impedance and the ability for zinc ions to reach the fiber surface more swiftly (**Figure** 5a). Furthermore, ANECF possessed the lowest charge transfer impedance, implying superior reaction kinetics. The tafel test also proved that ANECF has higher corrosion potential and lower corrosion current (Figure S5, Supporting Information). However, ANECF alone was not suitable for use as the cathode in flow batteries. Upon examination of ANECF removed from the AZIFB at the end of charging, it was observed that the surface was covered with a large amount of irregular and protruding white zinc (Figure 5b). In contrast, CF or CF equipped with ANECF exhibited more uniform surfaces with only a few indistinct white traces. This discrepancy may arise from the

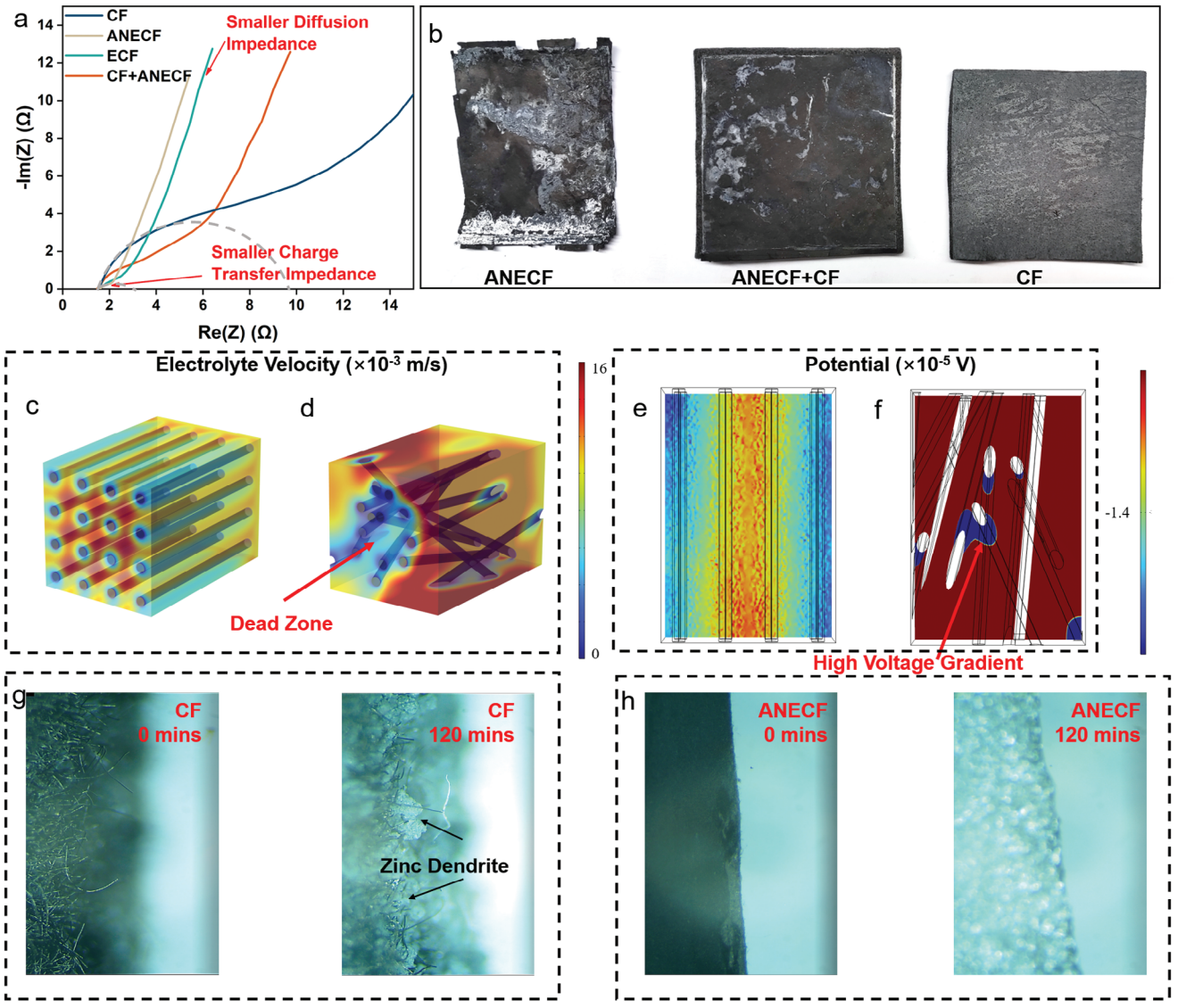

Figure 5. a) Nyquist curve of different carbon fiber electrodes. b) Photograph of different carbon fiber electrodes after charging. c,d) Electrode velocity distribution inside the electrode by COMSOL. e,f) Potential distribution inside the electrode by COMSOL. g,h) Zinc deposition image taken by in situ optical microscope at 10 mA cm^{-2}.

limited internal space of the thin ANECF, which was unable to accommodate excessive zinc deposition at high capacities, leading to the extrusion of excess zinc from within outward. Additionally, by integrating CF with ANECF, the underlying CF can utilize its larger pores to enhance the convection effects of the internal electrolyte, improving distribution uniformity and increasing the space available for zinc accommodation, thus preventing its outward growth. When CF and ANECF were stacked, although there was a slight increase in the charge transfer impedance, the low-frequency slope remained similar to that of ANECF, demonstrating that the enhancement in the mass transfer capability was not significantly affected. This configuration effectively combined the benefits of high surface area and reaction kinetics from ANECF with the structural and distribution advantages of CF, culminating in a novel and efficient electrode paradigm.

The improvement observed with ANECF over ECF was primarily due to its smaller pores reducing the diffusion distance of zinc ions on the electrode surface, thereby increasing the mass transfer rate. In addition to the enhanced mass transfer rate, the fiber alignment in ANECF can also improve the uniformity of electrolyte distribution and reaction. A simplified model was developed to evaluate the effect of fiber arrangement on the electrode performance by COMSOL. Given that the primary objective was to simulate the impact of an orderly fiber structure, the actual structure of the ANECF was simplified, neglecting the aggregation between fibers that existed in reality. The orderly fiber structure within ANECF allowed for a more uniform distribution of electrolyte flow velocity and reactant concentration (Figure 5c and Figure S6, Supporting Information). This implied that during the charge–discharge process, the electrode surface can maintain a consistent reaction rate, thereby suppressing the formation of

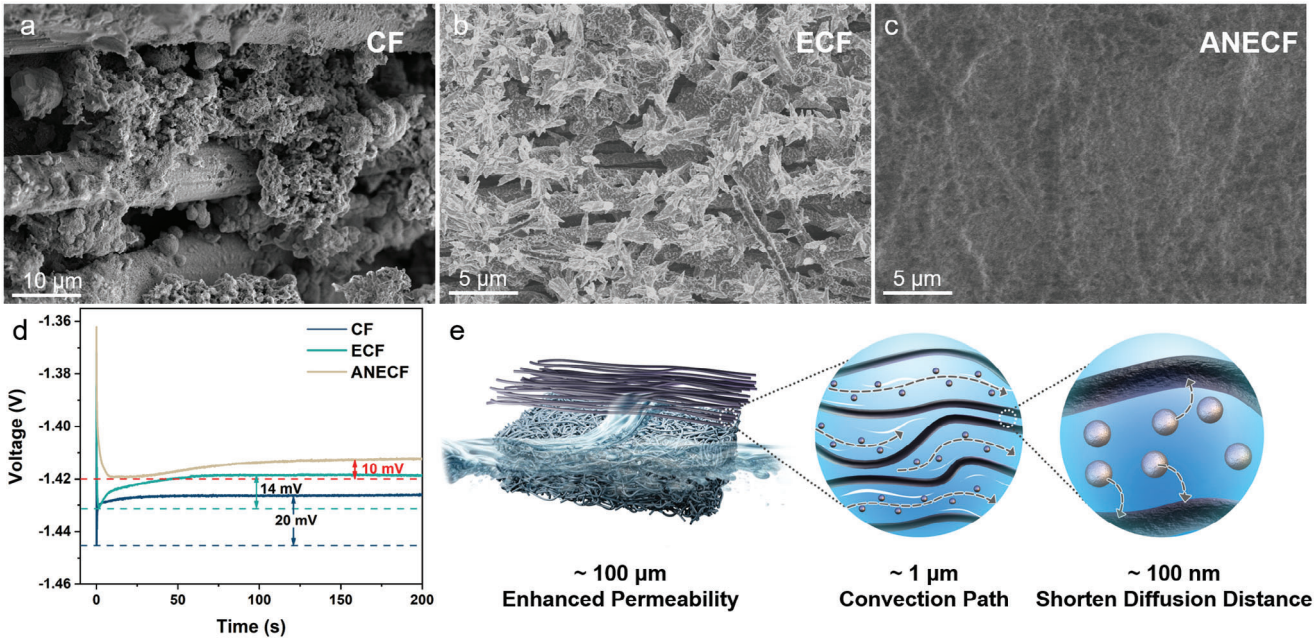

Figure 6. SEM images of a) CF, b) ECF, and c) ANECF after 30 min zinc deposition at 5 mA cm^{-2}. d) Nucleation overpotential of different materials. e) Working mechanism diagram of ANECF+CF composite electrode.

zinc dendrites. In contrast, the disordered fiber structure ECF led to a "dead zone" where electrolyte flow was restricted (Figure 5d), resulting in an uneven concentration distribution. Consequently, significant potential gradients emerge across certain areas of the electrode surface, as indicated in Figure 5f. On one hand, phase field simulations from previous studies have demonstrated that larger concentration gradients predisposed the formation of dendritic structures during zinc deposition.[42,43] On the other hand, the inhomogeneous distribution of the potential and concentration affects the mass transfer rate of zinc ions, which in turn exacerbates this dendritic growth phenomenon. The computational simulations using COMSOL software demonstrate that the uniformly aligned fiber structure and flow paths within the ANECF significantly enhance the uniformity of both concentration and current density, as presented in Figures S6 and S7 (Supporting Information). Although the surface of CF did not show obvious zinc deposition protrusion, the disordered structure inside CF had caused the agglomeration of uneven zinc deposition (Figure 5b). To more accurately observe the inhibitory effect of ANECF on the growth of zinc dendrites, in situ optical microscopy was utilized to capture the morphology of zinc deposition on different electrode materials at a current density of 10 mA cm^{-2} (Figure 5g,h, Videos S1 and S2, Supporting Information). The findings indicate that, as the deposition time elapsed, dendrites began to form within the CF matrix, with their height progressively increasing. The irregular porous structure resulted in an irregular morphology of zinc deposition. Conversely, the zinc deposition process on the ANECF was notably uniform, with the deposited zinc being smooth and evenly distributed across the electrode surface, devoid of significant dendrite growth or protrusions.

After zinc deposition, the surface of conventional CF was covered with zinc of various shapes and uneven distribution (**Figure 6a**). The zinc agglomerates, characterized by a loose and porous structure, filled the gaps between fibers, which can lead to the formation of a significant amount of "dead zinc" and promote the growth of zinc dendrites. This aggregated zinc not only disrupted the flow of electrolyte and current distribution but could also, in severe cases, form dendrites that puncture the membrane, affecting the safety of flow batteries. In the case of ECF, while there is no agglomeration of zinc between the fibers, the surface is covered with sharp zinc protrusions. The zinc distribution on ECF surfaces was relatively more uniform, a result of the small pore size that prevented zinc from agglomerating in the fiber gaps, instead accumulating gradually on the fiber surface (Figure 6b). However, the sharp and protruding zinc formations on the fiber surface were more likely to puncture the membrane, rendering ECF unsuitable for zinc-based flow batteries. Figure 6c illustrates that the zinc deposition within ANECF electrodes was flat. The deposited zinc formed a relatively uniform and flat plane within the fibers. This plane protected the membrane from being punctured by zinc dendrites. This type of deposition morphology is optimal, as it suppresses the growth of zinc dendrites and fully utilizes the areal capacity of the battery. One reason for the formation of such a morphological structure was the orderly fiber alignment, which led to more uniform zinc deposition. Another reason was that nitrogen doping can induce the formation of denser and finer nuclei during the initial stages of zinc deposition, thus preventing local zinc aggregation. The nucleation overpotential of the three materials was measured to substantiate this conclusion (Figure 6d). In electrochemical processes, overpotentials are the additional voltages required to drive the reactions beyond their thermodynamic equilibrium potentials. Specifically, nucleation overpotential and growth overpotential are two distinct phenomena that influence the kinetics of electrochemical reactions at the electrode/electrolyte interface.

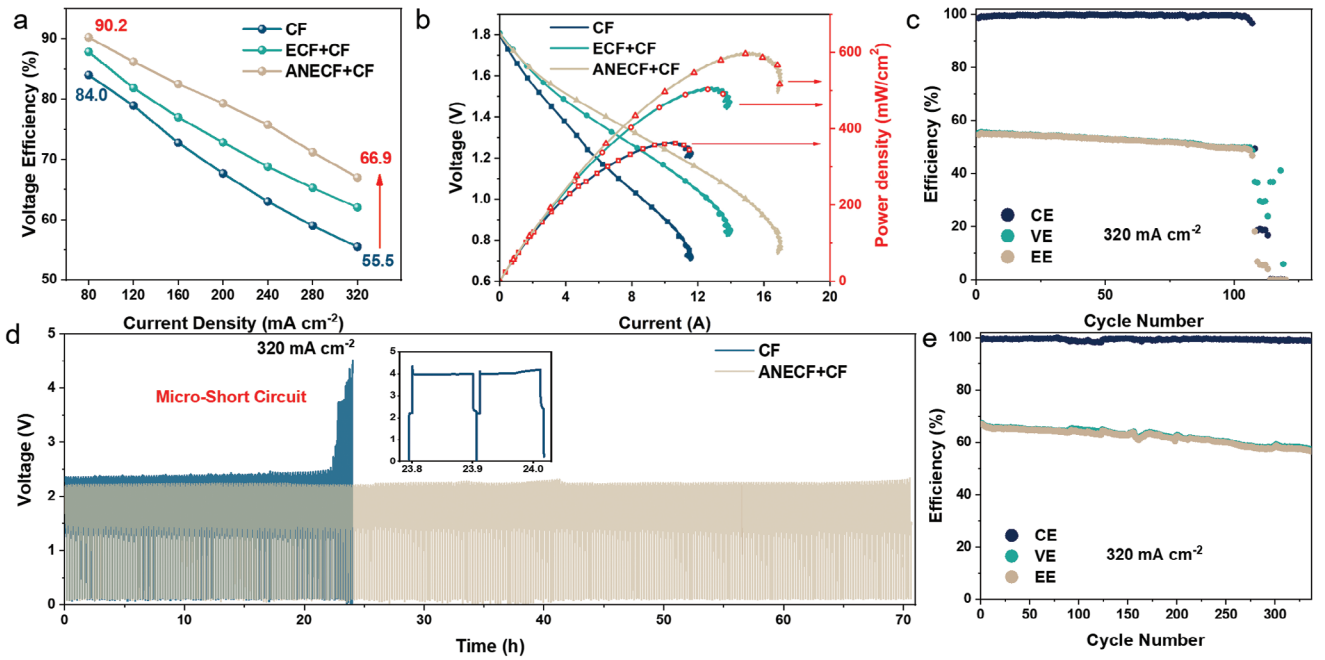

Figure 7. a) Voltage efficiency of AZIFB with different negative electrodes. b) Polarization curves and power densities curves of AZIFB with different negative electrodes. c) Battery efficiencies of AZIFB with CF electrode. d) Voltage profiles of AZIFB. e) Battery efficiencies of AZIFB with ANECF+CF electrode.

Nucleation overpotential refers to the energy barrier that must be overcome for the initial formation of reaction products on the electrode surface. The magnitude of nucleation overpotential is crucial in determining the onset of electrochemical reactions and can significantly affect the reaction rate and efficiency. A smaller nucleation overpotential means that more areas on the electrode surface can form nucleation sites. Growth overpotential, on the other hand, is the additional voltage needed to sustain the growth of the nucleated species or layers on the electrode surface. It is associated with the continuation of the electrochemical reaction beyond the nucleation stage. Growth overpotential is influenced by factors such as surface morphology, electrolyte composition, and the intrinsic properties of the electrode material. In ANECF, doping with nitrogen enhanced the binding energy between the electrode material and zinc atoms, leading to the formation of more zincophilic sites on the electrode surface, which in turn reduced the nucleation difficulty for zinc atoms. Among them, ANECF exhibited the smallest nucleation overpotential, which demonstrated that nucleation was least challenging on its surface.

For the ANECF+CF composite electrode, the hierarchical pore structure within it complemented each other's advantages, jointly enhancing electrode performance and deposition uniformity (Figure 6e). Electrolyte seeped into the carbon felt and achieved a high permeation rate and uniform distribution within the ≈100 µm pores through convection. After entering the ANECF, the electrolyte utilized the uniform large pore channels to achieve uniform distribution within the plane and rapid convection, and eventually, the ≈100 nm pores facilitated the rapid mass transfer of zinc ions. Once the zinc ions reached the fiber surface, the introduction of nitrogen elements ultimately led to relatively flat and uniform zinc deposition morphologies. This composite electrode achieved the dual functionality of enhanced ion transfer and suppression of zinc dendrite formation.

To thoroughly evaluate the influence of the ANECF+CF composite electrode on the performance of zinc-based flow batteries, a series of charge–discharge tests were conducted on single batteries fitted with varying negative electrode materials. Throughout these tests, the current was meticulously controlled and maintained at a constant level to ensure an accurate comparison of the battery's VE under different current densities. The results of the comparative analysis revealed a distinct pattern in VE among the different battery configurations. The CF demonstrated the lowest VE, which was typically indicative of higher polarization losses and less efficient energy conversion within the battery system (**Figure** 7a). On the other hand, the ANECF+CF composite electrode exhibited the highest VE, showcasing its superior ability to minimize polarization and maintain efficient energy transfer throughout the charge–discharge cycles. As the current density increased, the disparity in VE between the CF and ANECF+CF electrodes became more pronounced. At a moderate current density of 80 mA cm^{-2}, the difference in VE was relatively small at 6.2%. However, when the current density was raised to a more challenging level of 320 mA cm^{-2}, the gap in VE widened significantly to 11.4%. Thanks to its enhanced VE and a CE as high as 99.8%, even at a current density of 320 mA cm^{-2}, its EE could reach 66.9% (Table S3, Supporting Information). When the current density was only 80 mA cm^{-2}, EE could even reach 86.8%. This increase can be attributed to the heightened consumption rate of active ions at elevated current densities, which exacerbated the effects of any differences in mass transfer within the electrodes. This outcome was consistent with the data obtained from polarization curve analyses (Figure 7b and Figure S8, Supporting Information), further validating the performance benefits of the

composite electrode. Compared to conventional carbon felt, CF augmented with either ECF or ANECF demonstrated higher voltages at lower currents, which may be attributed to the increased specific surface area reducing the activation polarization of the electrode. The CF laminated with ANECF exhibited the highest limiting current and power density, a result that corroborates its significant enhancement in the mass transfer of active materials. The overall reduction in the concentration polarization led to a 45.3% increase in the limiting current density. The long-term cycling performance of the batteries further underscored the advantages of the ANECF+CF composite electrode. A notable issue encountered with the CF-based AZIFB was its poor cyclic stability under high current density conditions (Figure 7c,d). Specifically, the battery experienced a sudden voltage spike and subsequent failure after only 24 h of operation at 320 mA cm^{-2}, likely due to micro-short circuits caused by zinc dendrites that punctured the separator. This event underscored the critical challenge of zinc dendrite management in flow batteries and the potential risks it posed to battery stability and safety. In stark contrast, the AZIFB equipped with the ANECF+CF composite electrode demonstrated remarkable resilience, maintaining stable cycling for at least 70 h at the same high current density. The consistent performance of the battery was further evidenced by the minimal decay in various efficiencies. Extremely low attenuation can be maintained even at current densities up to 320 mA cm^{-2}. After 300 cycles, the battery could still maintain an EE of more than 59.2% (Figure 7e). This cycle life has surpassed the test data reported in the majority of literature on AZIFBs (Table S4, Supporting Information). The extended cycle performance at ultra-high current densities further corroborated the positive role of the novel electrode material in mitigating the growth of zinc dendrites. Although it does not represent the pinnacle of performance, taking into account the variations in experimental setups across different studies, it can be concluded that the material's cycle stability and its ability to suppress zinc dendrite growth have been adequately validated. This level of stability was highly desirable in practical applications, as it translated to a prolonged battery lifespan and sustained operational efficiency.

In summary, the comprehensive charge–discharge tests and long-term cycling assessments have reaffirmed the ANECF+CF composite electrode's exceptional cyclic stability and capacity to support long-term, efficient operation within zinc-based flow batteries. Although the experiments in this study were conducted solely under alkaline conditions, considering the structural stability of carbon fiber and the primary utilization of its microstructure in this research, it can be inferred that the application of the new electrodes in zinc-based redox flow batteries may be extended to acidic environments. These findings highlight the potential of the ANECF+CF composite electrode as a viable solution to overcome the challenges associated with zinc-based flow batteries and pave the way for more reliable and durable energy storage systems.

3. Conclusion

In conclusion, the comprehensive evaluation of the ANECF+CF composite electrode for zinc-based flow batteries has yielded promising results. The integration of the ANECF with conventional CF has demonstrated significant improvements in battery performance. The unique structural attributes of the ANECF+CF composite, including its innovative one-step manufactured dual-scale porous structure, have been instrumental in enhancing mass transfer, promoting uniform zinc deposition, and mitigating the formation of zinc dendrites. This represents a significant improvement over traditional methods, offering a more efficient and operable approach to electrode fabrication.

The composite structure integrated dual-scale pores within the same flow path in ANECF, with the underlying CF providing a high permeation rate. The innovative composite structure of ANECF+CF has demonstrated its advantages in charge–discharge testing. Compared to the traditional CF, the ANECF+CF composite electrode achieves higher VE across various current densities. Under more challenging conditions, the efficiency gap widens, reaching a maximum of 11.4%. Furthermore, the long-term cycling tests have revealed the superior stability of the ANECF+CF-based battery, which sustained operation for at least 70 h at a high current density of up to 320 mA cm^{-2} without significant efficiency decay or failure.

This composite electrode structure design represents a novel attempt in the realm of non-deposition flow batteries, and this work confirms the potential of this approach in the application of zinc-based flow batteries. Its ability to enhance electrochemical performance, improve cyclic stability, and reduce the risk of dendrite-related failures positions it as a promising candidate for advancing the development and commercialization of safe, efficient, and durable energy storage systems. The innovative approach and findings of this study are expected to inspire further research and development in the field of energy storage technology.

4. Experimental Section

Materials: Reagents required for electrospinning include PAN (MW ≈150 000), DMF, and melamine. KOH, NaOH, ZnO, and $Na_4Fe(CN)_6$ were required for the preparation of electrolytes. All of these were analytical reagents.

Preparation of Electrospun Carbon Fiber: PAN was dissolved in DMF to achieve a mass fraction of 10 wt%. The mixture was stirred for over 12 h to ensure complete dissolution. The resulting solution was then loaded into a syringe for electrospinning at a feeding rate of 1 mL h^{-1}. The applied voltage during the electrospinning process was 15 kV. The drum collector was set to rotate at a speed of 300 rpm and the spinning duration was ≈10 h. The as-spun film was subjected to a preliminary carbonization step at a temperature of 250 °C for 1 h. Following the preliminary carbonization, the film was further carbonized in a nitrogen atmosphere at 1000 °C for 1.5 h, also at a heating rate of 5 °C min^{-1}. Upon the completion of the carbonization process, the electrospun carbon fiber (ECF) was obtained. When the mass fraction of PAN was 8 wt% and that of melamine was 3 wt%, the drum collector's rotation speed was increased to 3000 rpm. The resultant carbonization process led to the formation of ANECF.

Material Characterization: XPS, XRD, and Raman spectroscopy were employed to characterize the properties of the materials. SEM and TEM were utilized to capture images of the materials' microstructures and morphological features. Mercury intrusion porosimetry (MIP) was conducted to measure the pore size distribution of the porous materials. The electrochemical properties of the materials were assessed in a standard three-electrode cell setup. The ECF and ANECF served as the working electrodes, with a platinum plate acting as the counter electrode and a saturated calomel electrode as the reference electrode. The cell was connected to an electrochemical workstation (VMP-3, BioLogic) for the experiments. CV was utilized to measure the ECSA of the electrode materials. EIS was

conducted to evaluate the interfacial properties and the kinetics of the electrochemical processes. Additionally, nucleation overpotential tests were performed to investigate the electrodeposition behavior of the materials.

Battery Test: In the battery testing procedure, an alkaline zinc-iron flow battery (AZIFB) with a reaction area of 5 cm by 5 cm was utilized. The negative electrode materials were CF, stacked ECF and CF (ECF+CF), and stacked ANECF and CF (ANECF+CF) respectively. The battery was connected to the Neware tester (CT-4008Tn) via two gold-plated copper plates. The positive and negative electrolyte solutions were composed of 0.8 mol L^{-1} $Fe(CN)_6^{4-}$ + 3 mol L^{-1} OH^- and 0.4 mol L^{-1} $Zn(OH)_4^{2-}$ + 3.8 mol L^{-1} OH^-, respectively. The volume of each electrolyte solution was 60 mL, which was circulated within the battery using a peristaltic pump. The method for calculating the flow rate of the electrolytes was referenced in the literature.[30] The charging process was terminated based on time (When the current density was 80 mA cm^{-2}, the charging time was 24 min), while the discharging process was halted when the voltage reached a specified cutoff point (0.1 V). The polarization curve of the battery was also measured using the electrochemical workstation.

Modeling: For ANECF, sixteen cylinders were set up in parallel to simulate the regular arrangement of fibers of ANECF. The gap between the fibers was set to 550 nm to mimic the actual pore size. A control volume of a rectangle of the appropriate volume was also taken to simulate the electrolyte. A Boolean difference operation was performed on the above geometric model to obtain the ANECF electrolyte model. For ECF, the arrangement of fibers which have an equal quantity with ANECF, were described using appropriate random numbers. More model details have been added in the Supporting Information.

Supporting Information

Supporting Information is available from the Wiley Online Library or from the author.

Acknowledgements

This work was supported by the Fundamental Research Funds for the Central Universities (grant number 2022ZFJH004), Hangzhou Science and Technology Commission (grant number 202204T13), and National Natural Science Foundation of China (grant number 51606164).

Conflict of Interest

The authors declare no conflict of interest.

Data Availability Statement

The data that support the findings of this study are available from the corresponding author upon reasonable request.

Keywords

electrospinning, flow battery, mass transfer, porous structure, zinc dendrite

Received: May 25, 2024
Revised: August 2, 2024
Published online:

[1] M. L. Perry, A. Z. Weber, *J. Electrochem. Soc.* **2015**, *163*, A5064.
[2] M. Park, J. Ryu, W. Wang, J. Cho, *Nat. Rev. Mater.* **2016**, *2*, 16080.
[3] R. F. Service, *Science* **2018**, *362*, 508.
[4] P. Wang, K. Zhang, H. Li, J. Hu, M. Zheng, *Small* **2023**, 2308791.
[5] J. Hu, P. Wang, J. Hu, M. Zheng, M. Dong, *Adv. Sci.* **2024**, 2401404.
[6] Q. Jian, Y. Wan, J. Sun, M. Wu, T. Zhao, *J. Mater. Chem. A* **2020**, *8*, 20175.
[7] Z. Xu, Q. Fan, Y. Li, J. Wang, P. D. Lund, *Renewable Sustainable Energy Rev.* **2020**, *127*, 109838.
[8] H. Zhang, W. Lu, X. Li, *Electrochem. Energy Rev.* **2019**, *2*, 492.
[9] W. Du, E. H. Ang, Y. Yang, Y. Zhang, M. Ye, C. C. Li, *Energy Environ. Sci.* **2020**, *13*, 3330.
[10] W. I. Jang, J. W. Lee, Y. M. Baek, O. O. Park, *Macromol. Res.* **2016**, *24*, 276.
[11] X. Shi, G. Xu, S. Liang, C. Li, S. Guo, X. Xie, X. Ma, J. Zhou, *ACS Sustainable Chem. Eng.* **2019**, *7*, 17737.
[12] Y. Du, X. Chi, J. Huang, Q. Qiu, Y. Liu, *J. Power Sources* **2020**, *479*, 228808.
[13] Q. Jian, Z. Guo, L. Zhang, M. Wu, T. Zhao, *Chem. Eng. J.* **2021**, *425*, 130643.
[14] P. Xue, C. Guo, L. Li, H. Li, D. Luo, L. Tan, Z. Chen, *Adv. Mater.* **2022**, *34*, 2110047.
[15] H. Bian, C. Wang, Y. Wang, Y. Ren, Y. Ge, H. Wu, B. Wang, D. Chen, B. Yang, D. Bin, Y. Li, J. Gu, Y. Ma, S. Tang, X. Meng, H. Lu, *Adv. Funct. Mater.* **2024**, *34*, 2401760.
[16] L. Zhou, W. Zhou, H. Wang, Q. Deng, X. Ai, X.-X. Zeng, X. Wu, C. Zhou, W. Ling, *Chem. Eng. J.* **2024**, *492*, 152324.
[17] P. Xiao, H. Li, J. Fu, C. Zeng, Y. Zhao, T. Zhai, H. Li, *Energy Environ. Sci.* **2022**, *15*, 1638.
[18] Z. Zhao, J. Zhao, Z. Hu, J. Li, J. Li, Y. Zhang, C. Wang, G. Cui, *Energy Environ. Sci.* **2019**, *12*, 1938.
[19] Y. Zhou, J. Xia, J. Di, Z. Sun, L. Zhao, L. Li, Y. Wu, L. Dong, X. Wang, Q. Li, *Adv. Energy Mater.* **2023**, *13*, 2203165.
[20] P. Xiong, Y. Zhang, J. Zhang, S. H. Baek, L. Zeng, Y. Yao, H. S. Park, *EnergyChem* **2022**, *4*, 100076.
[21] Y. Yang, C. Liu, Z. Lv, H. Yang, X. Cheng, S. Zhang, M. Ye, Y. Zhang, L. Chen, J. Zhao, C. C. Li, *Energy Storage Mater.* **2021**, *41*, 230.
[22] B. Sui, L. Sha, P. Wang, Z. Gong, Y. Zhang, Y. Wu, L. Zhao, J. Tang, F. Shi, *J. Energy Storage* **2024**, *82*, 110550.
[23] S. Huang, Z. Yuan, M. Salla, X. Wang, H. Zhang, S. Huang, D. G. Lek, X. Li, Q. Wang, *Energy Environ. Sci.* **2023**, *16*, 438.
[24] S. Xie, Y. Li, L. Dong, *J. Energy Chem.* **2023**, *76*, 32.
[25] H. Wang, Q. Li, S. Huang, L. Zhou, L. Mei, Z. Wu, B. Qu, W. Wei, X. Ji, Y. Chen, L. Chen, *Chem. Eng. J.* **2023**, *470*, 144147.
[26] C. Choi, J. B. Park, J. H. Park, S. Yu, D.-W. Kim, *Chem. Eng. J.* **2023**, *456*, 141015.
[27] B. Sui, L. Sha, Q. Bao, P. Wang, Z. Gong, M. Zhou, F. Shi, K. Zhu, *J. Colloid Interface Sci.* **2024**, *669*, 886.
[28] Y. Cheng, H. Zhang, Q. Lai, X. Li, D. Shi, L. Zhang, *J. Power Sources* **2013**, *241*, 196.
[29] M. H. Chakrabarti, N. P. Brandon, S. A. Hajimolana, F. Tariq, V. Yufit, M. A. Hashim, M. A. Hussain, C. T. J. Low, P. V. Aravind, *J. Power Sources* **2014**, *253*, 150.
[30] P. Wang, Y. Zhao, Y. Ban, M. Zheng, *J. Energy Storage* **2024**, *97*, 112859.
[31] W. Du, J. Yan, C. Cao, C. C. Li, *Energy Storage Mater.* **2022**, *52*, 329.
[32] L. Sha, B.-B. Sui, P.-F. Wang, Z. Gong, Y.-H. Zhang, Y.-H. Wu, L.-N. Zhao, J.-J. Tang, F.-N. Shi, *Chem. Eng. J.* **2024**, *481*, 148393.
[33] M. Sun, Z. Zhang, J. Chen, Y. Zhang, R. Wang, H. Mu, C. Lian, W. Wang, G. Wang, *Chem. Eng. J.* **2023**, *474*, 145658.
[34] Z. Kang, C. Wu, L. Dong, W. Liu, J. Mou, J. Zhang, Z. Chang, B. Jiang, G. Wang, F. Kang, C. Xu, *ACS Sustainable Chem. Eng.* **2019**, *7*, 3364.
[35] J. Sun, H. R. Jiang, B. W. Zhang, C. Y. H. Chao, T. S. Zhao, *Appl. Energy* **2020**, *259*, 114198.
[36] Q. Wu, Y. Lv, L. Lin, X. Zhang, Y. Liu, X. Zhou, *J. Power Sources* **2019**, *410*, 152.

[37] R. Wang, M. Hao, C. He, Z. Tu, F. Chong, Y. Li, *Appl. Catal., B* **2023**, *332*, 122773.
[38] L. Lu, X. Cao, Z. Shen, L. Li, J. Huo, W. Chen, C. Liu, H. Liu, *Sustainable Mater. Technol.* **2020**, *26*, 00221.
[39] Q. Cao, H. Gao, Y. Gao, J. Yang, C. Li, J. Pu, J. Du, J. Yang, D. Cai, Z. Pan, C. Guan, W. Huang, *Adv. Funct. Mater.* **2021**, *31*, 2103922.
[40] J. Zhou, M. Xie, F. Wu, Y. Mei, Y. Hao, R. Huang, G. Wei, A. Liu, L. Li, R. Chen, *Adv. Mater.* **2021**, *33*, 2101649.
[41] Y. Zeng, P. X. Sun, Z. Pei, Q. Jin, X. Zhang, L. Yu, X. W. (David) Lou, *Adv. Mater.* **2022**, *34*, 2200342.
[42] K. Wang, Y. Xiao, P. Pei, X. Liu, Y. Wang, *J. Electrochem. Soc.* **2019**, *166*, D389.
[43] B. Pant, Y. Ren, Y. Cao, *ACS Appl. Mater. Interfaces* **2023**, *15*, 59329.